

Supplementary Information for

Plumbing the depths of magma crystallization using $^{176}\text{Lu}/^{177}\text{Hf}$ in zircon as a pressure proxy

Hugo Moreira*, Anda Buzenchi, Chris J. Hawkesworth, Bruno Dhuime

Email: hugo.moreira@umontpellier.fr

This PDF file includes:

Supplementary text
Figures S1 to S8
Tables S1 to S9
Legends for Datasets S1 to S4
SI References

Other supplementary materials for this manuscript include the following:

Datasets S1 to S4

Supplementary Information Text – Methods

Global datasets for Lu-Hf and O isotopes in zircon

Data sources. For Lu-Hf isotopes, the dataset from Puetz and Condie (2019) (i.e., a worldwide compilation of 119,422 analyses) was selected. Data from 25 papers (5,143 analyses) were added to this global dataset, and eighty-nine analyses with $^{176}\text{Lu}/^{177}\text{Hf}$ ratios equal or below zero were discarded. For oxygen isotopes, the global database from Spencer et al. (2014) (6,372 zircon analyses) was selected. Each 0.1 Gyr interval of the two datasets was filtered by rejecting individual points that fall outside the 2 standard deviations (s.d.) of the median values obtained from the unfiltered data (**Table S1** and **S2**). This reduced the Lu-Hf dataset to 109,837 analyses and the oxygen isotopes dataset to 6,294 analyses (**Dataset S1**).

Non gaussian distribution occurs when a dataset approach low absolute values, such as $^{176}\text{Lu}/^{177}\text{Hf}$ values. To avoid this, the total dataset of 124,476 was subtracted by low values classified as metamorphic (7,246 zircon grains have values <0.0003 , see approach below) and the geometric mean was calculated for the data separated in 0.1 Gyr intervals (**Table S2**). The compilations are presented in **Dataset S1**. We used the *ggplot* data visualization package in R programming language for plotting the global density distribution of $^{176}\text{Lu}/^{177}\text{Hf}$ values divided by 0.1 Gyr intervals (**Fig. S1**).

Reverse correlation in Figure 1. Using time slice values and errors for the $^{176}\text{Lu}/^{177}\text{Hf}$ and oxygen datasets (**Table S1** and **S2**) we calculated a running mean for each period composed of one time slice and its two adjacent (younger and older) time slices (i.e., 5 values to derive the mean for each time slice). The first and last median values for the $^{176}\text{Lu}/^{177}\text{Hf}$ and oxygen datasets only take in consideration the two forward and two precedent times slices (i.e., 3 values to derive the running mean). The difference between the calculated running mean and the correspondent time slice then configures the ‘anomaly’ symbolised as Δ (**Table S3**). The anomalies of each time slice are then compared to the 1 s.d. of the $^{176}\text{Lu}/^{177}\text{Hf}$ and oxygen datasets. If the absolute values of the anomalies are larger than the 1 s.d. for both datasets, the time slice is chosen. The collection of chosen anomaly pairs between the $^{176}\text{Lu}/^{177}\text{Hf}$ and oxygen datasets define the negative trend presented in the **Figure 1**. The uncertainties for the anomaly pairs are the 2 standard errors (s.e.) of the correspondent time slice variable (Y-axis for $^{176}\text{Lu}/^{177}\text{Hf}$ and X-axis for $\delta^{18}\text{O}$ medians). The slope of the line

on the plot is significant at the 95% level, showing that for those time slice points, the $\delta^{18}\text{O}$ and $^{176}\text{Lu}/^{177}\text{Hf}$ pairs appear anomalous and also inversely correlate (i.e., when $\delta^{18}\text{O}$ is high, $^{176}\text{Lu}/^{177}\text{Hf}$ is low).

Change point analysis. Change point analysis was performed using *strucchange* and *breakpoints* packages of R programming language to identify multiple existing change points in the global database. By default, a maximum number of breaks was used based on the number of observations in each segment of 0.1 Gyr bins. The Bayesian information criterion (BIC) and the residual sum of squares (RSS) return 2 major breaking points in the datasets and the maximum of 6 possibilities of breaking points (**Fig. S2, S3 and S4**). Structural breaks in cumulative sum of median values (herein ascribed as second order variations) are identified for both $^{176}\text{Lu}/^{177}\text{Hf}$ and $\delta^{18}\text{O}$ datasets at ca. 3.8 Ga, 3.15 Ga, 2.56 Ga, 1.95 Ga, 1.24 Ga and 0.63 Ga (**Table S4**).

We also used CUSUM (cumulative sum control chart) and bootstrap analysis through the package Change point analyzer (<http://www.variation.com/cpa>). It detects multiple changes and provides both confidence levels and confidence intervals for each change, besides performing bootstrapping of the uploaded dataset. Different levels of confidence can be used to attribute the breaking points. For both $^{176}\text{Lu}/^{177}\text{Hf}$ and $\delta^{18}\text{O}$ isotopes datasets, we realized 1,000,000 bootstraps in the samples with 68 and 95% confidence intervals (**Tables S5, S6, S7 and S8**). When a lower confidence interval is considered (68%), coherent statistical variations for both $\delta^{18}\text{O}$ and $^{176}\text{Lu}/^{177}\text{Hf}$ data are observed at 3.0 ± 0.25 Ga, 1.85 ± 0.1 Ga, 1.3 ± 0.1 Ga, 1.0 ± 0.05 Ga and 0.65 ± 0.1 Ga. Overall, the change point analysis and the second order variations yield reasonably similar results, although breaks at 3.8 Ga and 2.56 Ga are only identified in the latter.

Zircon Lu-Hf geochemical pressure proxy

Data sources. References for the compiled dataset used to build equation (1) are presented in **Dataset S2**. Independent approaches for estimating the pressure of magma emplacement or generation comprise mainly Al-in-hornblende barometry but also examples of phase equilibria-based pressure of igneous mineralogy or in the wall rocks surrounding a granitoid body, and depths estimates based on geochemical composition and experimental petrology. These were plotted against the geometric mean of $^{176}\text{Lu}/^{177}\text{Hf}$ values of zircons interpreted to have crystallized in the host igneous rocks (**Dataset S2**). Seventy samples from the igneous dataset were used to constrain the equation (1).

Analogous data from metamorphic zircons of 44 samples were also compiled, and they show characteristically lower $^{176}\text{Lu}/^{177}\text{Hf}$ than igneous zircons. This difference in $^{176}\text{Lu}/^{177}\text{Hf}$ in igneous and metamorphic zircon is taken to reflect the widespread occurrence of garnet as a co-existing phase during zircon growth in metamorphic samples (**Dataset S2**). One metamorphic data point plots distinctively far above the metamorphic trend and was treated as an outlier (**Fig. 2**). In this specific sample, zircon domains that contain coesite inclusions (and have crystallized above > 2.5 GPa) have much higher $^{176}\text{Lu}/^{177}\text{Hf}$ because they grew in an unusual Ca-poor quartzose metasedimentary composition matrix where garnet was not part of the mineralogy.

Uncertainties. Errors are the calculated 2 s.e. of the $^{176}\text{Lu}/^{177}\text{Hf}$ analyses, and only $^{176}\text{Lu}/^{177}\text{Hf}$ ratios with at least 6 significant figures provided were considered. For the pressure (in GPa), if uncertainties were not provided in the source study, we used the mean pressure for a range in pressure conditions and the difference between the mean and the maximum pressure was taken as the uncertainty. When no pressure range was available, 10% of the pressure value was assumed to correspond to the pressure uncertainty. For volcanic samples, we used 0.02 ± 0.01 GPa to allow for crystallization taking place near the Earth's surface.

Equations. Because the $^{176}\text{Lu}/^{177}\text{Hf}$ and GPa data define an exponential relationship, we undertook equation uncertainty analysis by plotting the logarithm of GPa vs. $^{176}\text{Lu}/^{177}\text{Hf}$, which produces a linear array amenable to linear regression using individual datapoint uncertainties via Isoplot (Ludwig, 2003). The uncertainty envelopes at 95% confidence were then transformed back into the GPa vs. $^{176}\text{Lu}/^{177}\text{Hf}$ plot and are shown on our **Figure 2**. The equations are given below:

$$\text{Best fit: GPa}_{(\text{sample})} = e^{(^{176}\text{Lu}/^{177}\text{Hf}_{(\text{zircon})} - 0.000711)/(-0.000343)}$$

$$\text{Lower envelope: GPa}_{(\text{sample})} = e^{(^{176}\text{Lu}/^{177}\text{Hf}_{(\text{zircon})} - 0.000625)/(-0.000320)}$$

$$\text{Upper envelope: } \text{GPa}_{(\text{sample})} = e^{(^{176}\text{Lu}/^{177}\text{Hf}_{(\text{zircon})} - 0.000779)/(-0.000368)}$$

If emplacement estimates only are used for fitting, the following equations are produced (red curve in **Fig. 2b**):

$$\text{Best fit: } \text{GPa}_{(\text{sample})} = e^{(^{176}\text{Lu}/^{177}\text{Hf}_{(\text{zircon})} - 0.000631)/(-0.000374)}$$

$$\text{Lower envelope: } \text{GPa}_{(\text{sample})} = e^{(^{176}\text{Lu}/^{177}\text{Hf}_{(\text{zircon})} - 0.000518)/(-0.000347)}$$

$$\text{Upper envelope: } \text{GPa}_{(\text{sample})} = e^{(^{176}\text{Lu}/^{177}\text{Hf}_{(\text{zircon})} - 0.000726)/(-0.000403)}$$

The $^{176}\text{Lu}/^{177}\text{Hf}$ of metamorphic and igneous zircons. A histogram plotting all igneous zircon $^{176}\text{Lu}/^{177}\text{Hf}$ from our calibration dataset show that <2% of all zircons fall below a $^{176}\text{Lu}/^{177}\text{Hf}$ value of 0.0003 (**Fig. 2b**). In contrast, metamorphic zircons plotted below in the pressure range 0.5->2.0 GPa are mainly <0.0005 with the majority falling <0.0003 (~87%). Despite a modest overlap between these histograms, zircons with $^{176}\text{Lu}/^{177}\text{Hf}$ <0.0003 are likely / highly likely metamorphic. We regard ‘metamorphic’ data with $^{176}\text{Lu}/^{177}\text{Hf}$ >0.0003 as ambiguous since in the studies we used, many of these involve anatectic conditions, meaning that while solid state growth of zircon has widely occurred, some analysed zircon domains may represent crystallization from partial melt. On this basis, it is concluded that (1) some of the $^{176}\text{Lu}/^{177}\text{Hf}$ ratios at ‘Barrovian’ pressures (0.5-0.8 GPa) may reflect ‘igneous’ zoning that overlap more than they should with the lower range of igneous zircons, and (2) the quality of the metamorphic calibration could be improved with further studies of $^{176}\text{Lu}/^{177}\text{Hf}$ in zircon reflecting only 100% solid state growth in the lower range of pressure, (3) a cut off between metamorphic and igneous zircons at 0.0003 is a reasonable first order differentiation, and (4) due to the presence of analyses with $^{176}\text{Lu}/^{177}\text{Hf}$ ratios in the range of ‘Barrovian’-type metamorphism, the final $^{176}\text{Lu}/^{177}\text{Hf}$ ratios of 0.1 Gyr bins could be slightly biased towards lower values and thus comprise minimum estimates. Nonetheless, even if the dataset is filtered at $^{176}\text{Lu}/^{177}\text{Hf}$ <0.0008 instead, theoretically removing all the metamorphic zircons from the dataset, the peaks and troughs in zircon $^{176}\text{Lu}/^{177}\text{Hf}$ persist over time. Such an approach should be considered extreme as ~40% of the data is filtered, which is at odds with proportions estimates for igneous and metamorphic zircons in the global zircon record (e.g., Balica et al., 2020). Moreover, a further assessment shows that peaks and troughs also persist over time when the global dataset is divided into quartiles (**Fig. S5**), indicating that the oscillations of the lowest $^{176}\text{Lu}/^{177}\text{Hf}$ values are not an artefact due to the contribution of metamorphic zircons. Th/U ratios were not used for filtering because i) these ratios are not available in the global dataset compiled by others; ii) it has been demonstrated that metamorphic zircon does not always have low Th/U, and this ratio should only be used as a complementary approach for identifying metamorphic zircon (Rubatto, 2017).

Modelling the behavior of Lu and Hf in zircon

To model the trend inferred from the equation (1), we first calculated the $^{176}\text{Lu}/^{177}\text{Hf}$ of melts generated after partial melting of three types of source rocks: a N-MORB basalt, an Archean basalt and a TTG with respective bulk-rock $^{176}\text{Lu}/^{177}\text{Hf}$ ratios of 0.031, 0.017 and 0.008. The TTG composition is derived from the partial melting model of the Archean basalt (Gardiner et al., 2018). We used a batch partial melting model (Rollinson and Pease, 2021), modal proportion of residual phases from Gardiner et al. (2018) and mineral/melt partition coefficients for Lu, Hf and Yb of **Table S9**. Upon partial melting, the $^{176}\text{Lu}/^{177}\text{Hf}$ of the melt decreases when the pressure is high enough for garnet to be present in large amounts in the residue (**Fig. S6a**). We took the $^{176}\text{Lu}/^{177}\text{Hf}$ of melt produced by 5% partial melting of the different compositions and modelled different crystallization assemblages as the melt fraction increases. The $^{176}\text{Lu}/^{177}\text{Hf}$ of crystallizing zircons was obtained by empirical partition coefficients between zircon and host igneous rocks ($^{176}\text{Lu}/^{177}\text{Hf}_{\text{zircon}}/^{176}\text{Lu}/^{177}\text{Hf}_{\text{melt}}$, **Dataset S2**). Successful models, i.e., those that overlap the global composition of Yb vs. $^{176}\text{Lu}/^{177}\text{Hf}$ compositions (**Fig. 3a**), demonstrate that the $^{176}\text{Lu}/^{177}\text{Hf}$ of crystallizing zircons is lower with increasing volume of melt and increase of garnet as a residual phase.

The lowest $^{176}\text{Lu}/^{177}\text{Hf}$ of melt produced by 15% partial melting of the TTG composition ($^{176}\text{Lu}/^{177}\text{Hf}$ = 0.000312) is used to model batch crystallization. Invariably, the $^{176}\text{Lu}/^{177}\text{Hf}$ of the remaining melt is lower than the initial composition, except when zircon is one of the crystallizing phases. The results indicate that

when zircon saturation is reached, the $^{176}\text{Lu}/^{177}\text{Hf}$ of the melt becomes higher (**Fig. S6b**). In a closed system, the $^{176}\text{Lu}/^{177}\text{Hf}$ of the melt will then progressively decrease if incremental crystallization processes are involved (**Fig. S5b**). If crystals are instead fractionated (i.e., extracted from the equilibrated melt) and consecutive fractionation steps are performed, the remaining $^{176}\text{Lu}/^{177}\text{Hf}$ of the melt (**Fig. S6c**) and the $^{176}\text{Lu}/^{177}\text{Hf}$ of zircons crystallizing from it (**Fig. 3b**), exponentially increase due to efficient removal of Hf by zircon fractionation. Additional information is provided in **Dataset S3**.

Assumptions involved in the models are: (1) The partition coefficients between garnet, zircon and 'reservoir' (i.e., matrix phases during growth) are assumed to remain constant. In practice this is not always true because the composition of the minerals and their modal abundances change during growth. Consequently, the full volume of garnet and zircon may not be in equilibrium. (2) Elemental zoning (e.g., variations in Lu contents) in garnet is ignored. (3) Temperature in metamorphic reactions or crystallizing systems is not considered as a controlling factor in the assimilation of Lu by either garnet or zircon. The preferential uptake of HREE in garnet relative to zircon is a common empirical observation, although a few experiments show higher partition coefficient experiments for zircon grains at the range of 1000–900 °C and 20 kbar (Taylor et al., 2015). Even in those cases of higher HREE zircon partition coefficient, the equilibrium between zircon and garnet yielded zircon profiles depleted in Lu. (4) The maximum abundance of zircon is controlled by the concentration of Zr and Hf (usually <0.05% by volume in a rock).

Temperature and composition dependence

Considering Ti-in-zircon as a temperature indicator (e.g., Ferry and Watson, 2007), we evaluate the temperature and melt K_d 's dependence in zircon $^{176}\text{Lu}/^{177}\text{Hf}$ by using the dataset in **Figure 3** and the $\text{Lu}_{\text{Kd}}/\text{Hf}_{\text{Kd}}$ (Claiborne et al., 2018) plotted separately against the Ti concentration (**Fig. S7**). Besides the absence of a trend between zircon $^{176}\text{Lu}/^{177}\text{Hf}$ and Ti, a range of Ti concentrations from 5 – 25 ppm reflecting temperatures of magmas between (700 - 850 °C) show a maximum effect of 1.5 times the $^{176}\text{Lu}/^{177}\text{Hf}$ ratio; which is a much minor effect compared to the processes presented in **Figure 3**.

The geochemical information of igneous samples from **Dataset S2** was evaluated to check whether variations in zircon $^{176}\text{Lu}/^{177}\text{Hf}$ can be attributed to compositional changes. Although a trend between SiO_2 and Lu/Hf whole-rock exists (**Fig. S8a**, after 3 outliers removed), the same samples do not show a trend between SiO_2 and the zircon $^{176}\text{Lu}/^{177}\text{Hf}$ (**Fig. S8b**). There is a weak trend between zircon $^{176}\text{Lu}/^{177}\text{Hf}$ vs whole-rock Lu/Hf that hint towards a dependence between zircon and crystallizing magma composition (**Fig. S8c**, after outliers rejected), but this trend alone can only account for a very minor change in zircon $^{176}\text{Lu}/^{177}\text{Hf}$ (~3 times). Additionally, the dataset shows that zircon $^{176}\text{Lu}/^{177}\text{Hf}$ do not vary significantly with sample age (**Fig. S8d**), and by implication, it suggests that secular compositional variations through time do not play a major control in changing the global zircon $^{176}\text{Lu}/^{177}\text{Hf}$ presented in **Figure 1**.

Converting pressure to crustal depth (km)

Lithostatic pressure or overburden stress is considered as the pressure imposed by a vertical column of overlying rock described as:

$$P = \rho g z$$

where P is pressure in MPa, ρ is density in kg.m^{-3} , g is gravity (constant as 9.81 m.s^{-2}) and z is the depth in m.

Conversion from pressure to depth depends upon the average density of the rock column above the given pressure, and this can vary from 2650–2900 kg.m^{-3} depending on whether the column consists of mafic, felsic, metamorphic or sedimentary rocks. We used a value of 2.8 g.cm^{-3} that is typical for the bulk continental crust (Christensen and Mooney, 1995). The processed data used to plot the mean depth of magmas crystallization through time is presented in **Dataset S4**.

Supercontinents

In the light of the statistical variations between zircon $^{176}\text{Lu}/^{177}\text{Hf}$ troughs and $\delta^{18}\text{O}$ peaks, and previous estimates in the literature (Campbell and Allen, 2008; Bradley et al., 2011; Pastor-Galan et al., 2009; Condie

et al., 2021 in **Fig. 1**), we framed the periods of supercontinent assembly as 0.18–0.35; 0.55–0.75; 1.05–1.3; 1.9–2.1; 2.45–2.75 Ga, respectively for Pangea, Gondwana, Rodinia, Nuna and Kenor. The oscillations in the isotopic ratios observed in this study, alongside cycles of typically 0.5–0.6 Gyr, are thus interpreted as best estimates for supercontinent assembly, as presented by the orange bars in **Figure 4**.

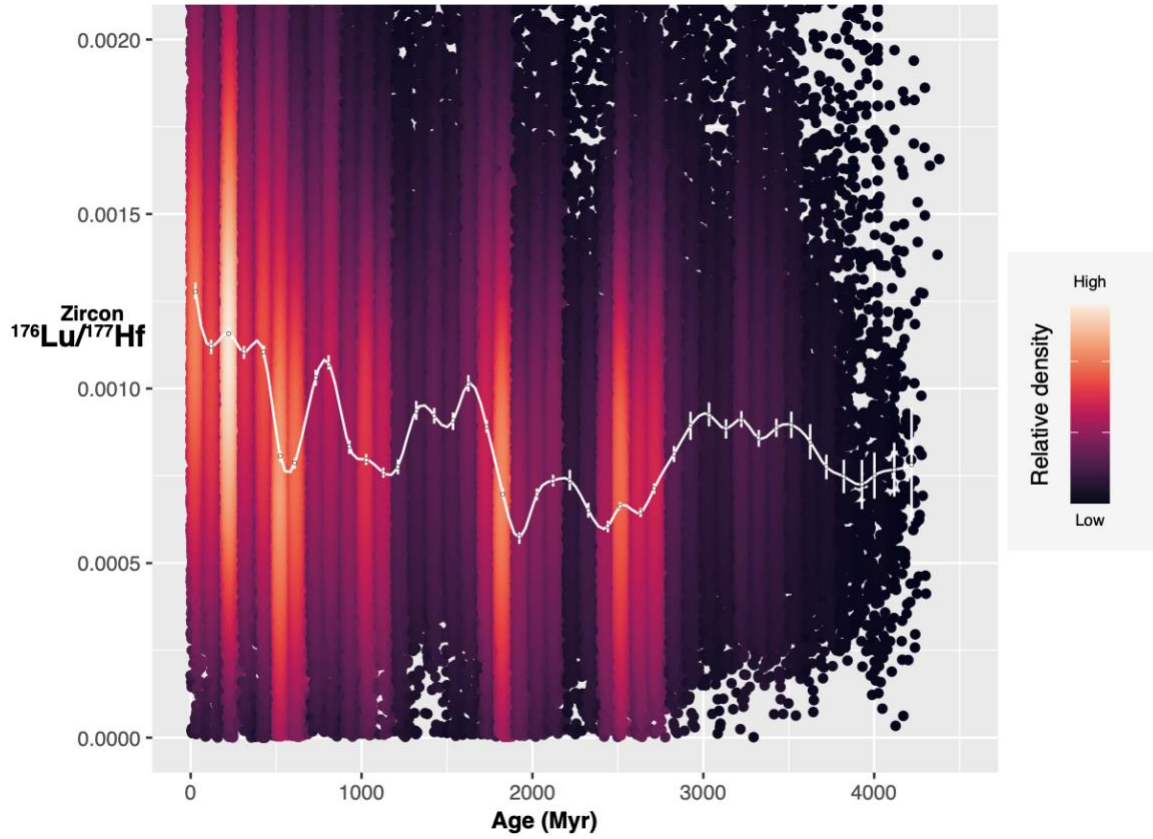


Fig. S1. Relative density plot of the global $^{176}\text{Lu}/^{177}\text{Hf}$ dataset divided in 0.1 Gyr intervals. Each of the 0.1 Gyr bands shows a highest density region (marked by lighter colours) where most of the $^{176}\text{Lu}/^{177}\text{Hf}$ values plot for that specific age range. The density is comparable among the 0.1 Gyr bands; i.e., it allows one to observe the relative number of samples per interval. The white curve is the geometric mean for igneous zircon data (also plotted in **Fig. 1**).

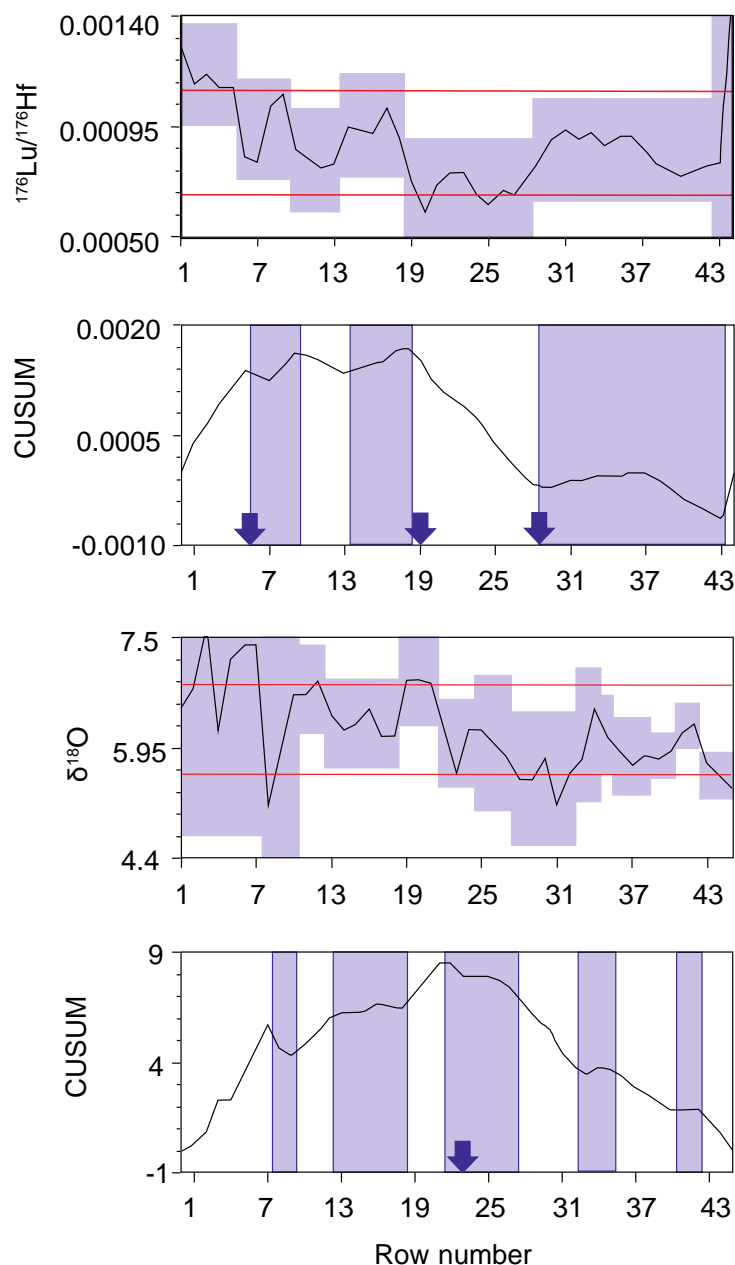


Fig. S2. $^{176}\text{Lu}/^{177}\text{Hf}$ and $\delta^{18}\text{O}$ time series with breaking points higher than 68% confidence marked by the edges of the purple bars. Every time a purple bar displaces up or down, it indicates that a change of point analysis was detected. Red horizontal lines indicate control limits. They represent the maximum range that the values are expected to vary over assuming no change has occurred. Points outside the control limits indicate a change has occurred. The 95% confidence breakpoints are marked by dark purple arrows. CUSUM are the cumulative sum of the values and indicate points of inflexion marked as structural breaks to the dataset. Values on the X-axis correspond to the row key indicated in **Table S1**.

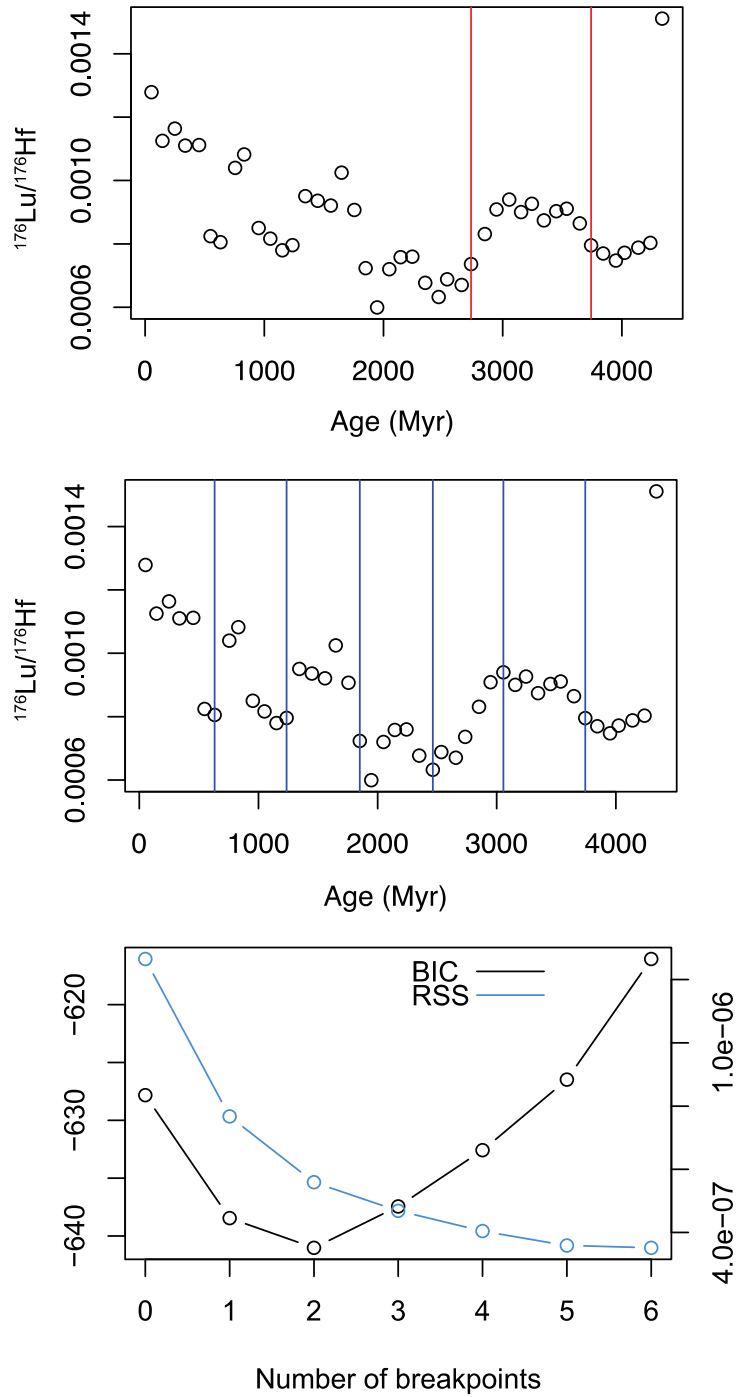


Fig. S3. Breaking points at 2 observation points (following BIC lowest) and breaking points at 6 observation points (following RISS lowest). BIC analyses of Lu/Hf at the bottom indicate 2 major breakpoints (2.8 and 3.8 Gyr) and RSS indicate maximum breakpoints at 6 observations (second order variations).

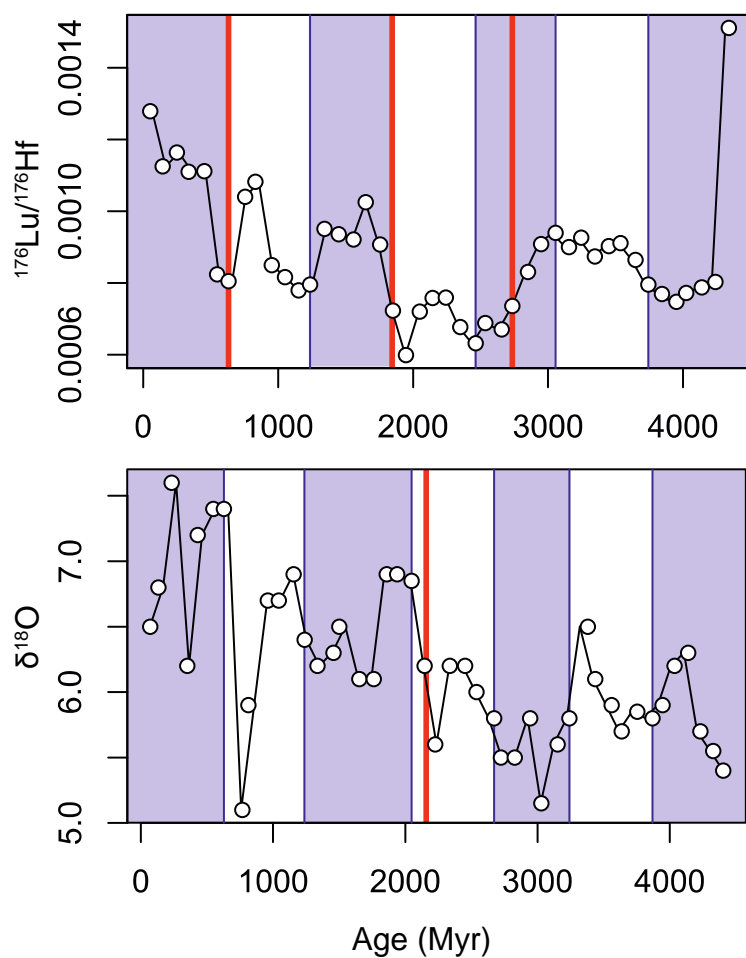


Fig. S4. Second order variations for $^{176}\text{Lu}/^{177}\text{Hf}$ and $\delta^{18}\text{O}$ isotopes are represented by the edges of the purple bars. For comparison, the major breakpoints using 95% confidence are also represented in red.

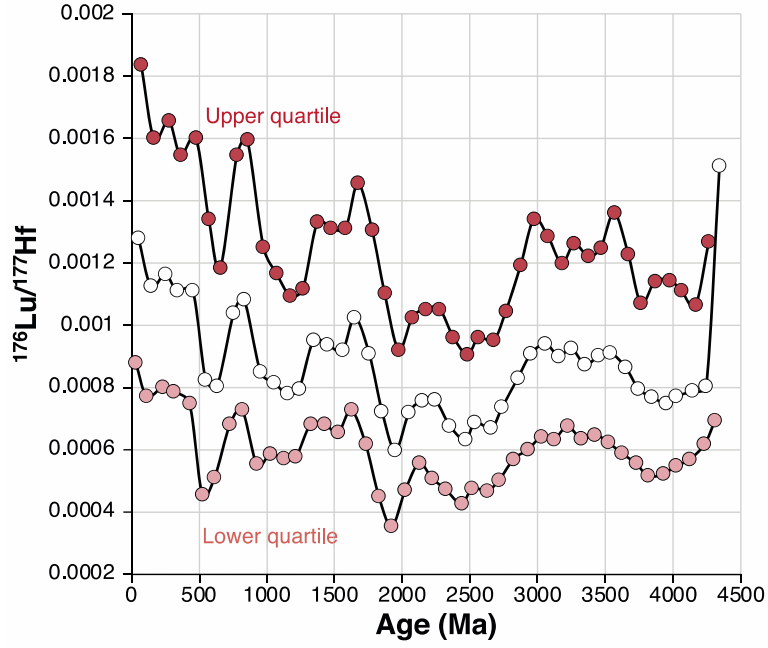


Fig. S5. The upper and lower quartiles of the global zircon $^{176}\text{Lu}/^{177}\text{Hf}$ dataset show similar oscillations through time compared to the median $^{176}\text{Lu}/^{177}\text{Hf}$ values.

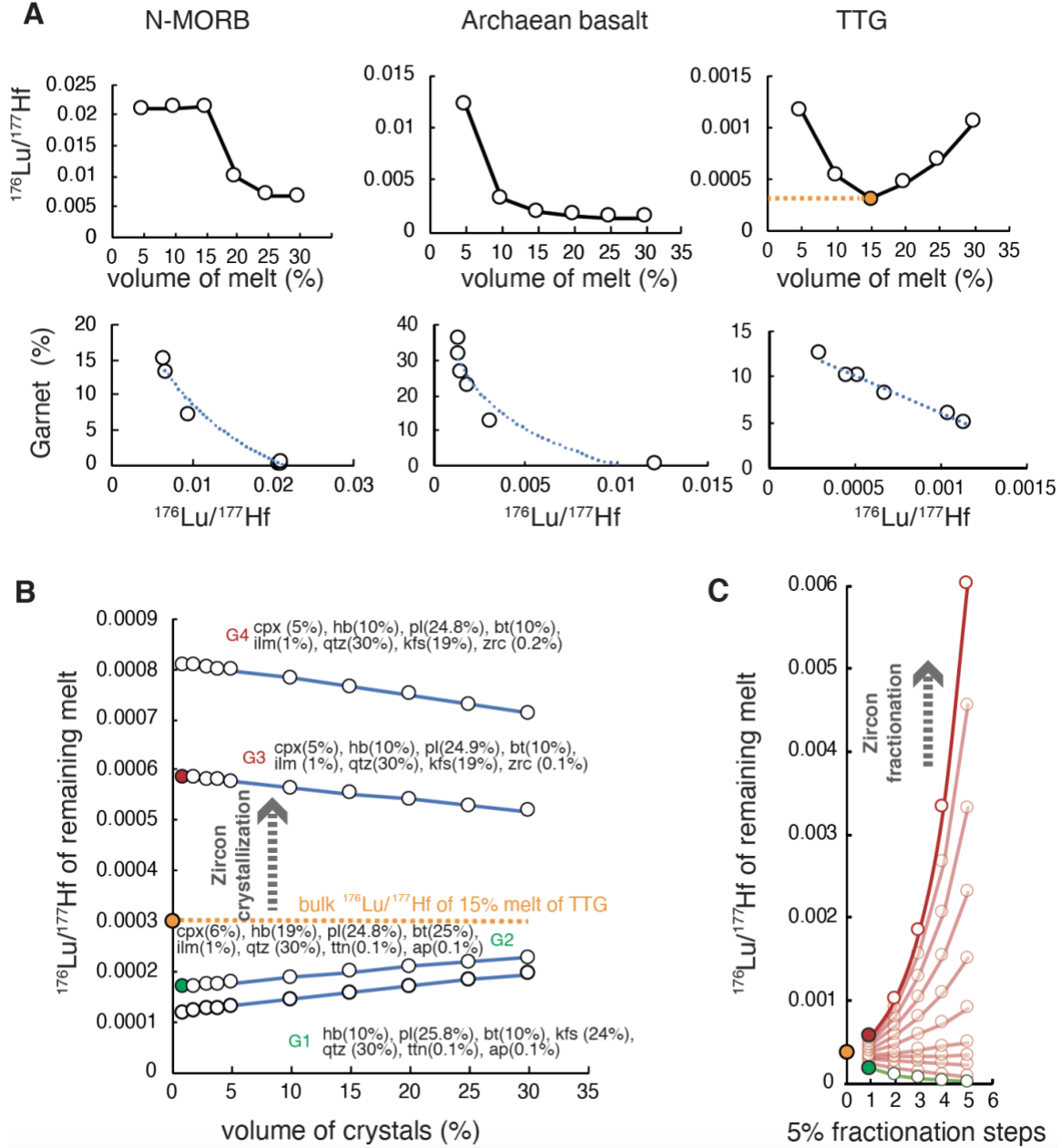


Fig. S6. Influence of garnet and zircon on $^{176}\text{Lu}/^{177}\text{Hf}$ ratios. A) Upper diagrams: Evolution of the $^{176}\text{Lu}/^{177}\text{Hf}$ ratios in a melt for three different sources as a function of the degree of melting. Lower diagrams: Melt $^{176}\text{Lu}/^{177}\text{Hf}$ ratio dependence on the abundance of garnet as a residual phase. The orange dot indicates the $^{176}\text{Lu}/^{177}\text{Hf}$ of the TTG-derived melt used for the batch crystallization modelling presented in B. B) Model of $^{176}\text{Lu}/^{177}\text{Hf}$ of a melt (orange dot) in equilibrium with four different crystallizing mineral assemblages (closed system). This model highlights the dramatic effect that zircon has on shifting $^{176}\text{Lu}/^{177}\text{Hf}$ ratios to higher values. C) Two of the crystallizing assemblages Qtz+Plg+Kfs+Amp+Bt+Cpx+Ilm+Ap+Ttn, in red (zircon present) and green (zircon absent), are then modelled to consecutively fractionate and remove the crystallizing assemblages from the remaining melt (open system). Higher $^{176}\text{Lu}/^{177}\text{Hf}$ are produced when zircon is fractionated but $^{176}\text{Lu}/^{177}\text{Hf}$ remains low if zircon is absent.

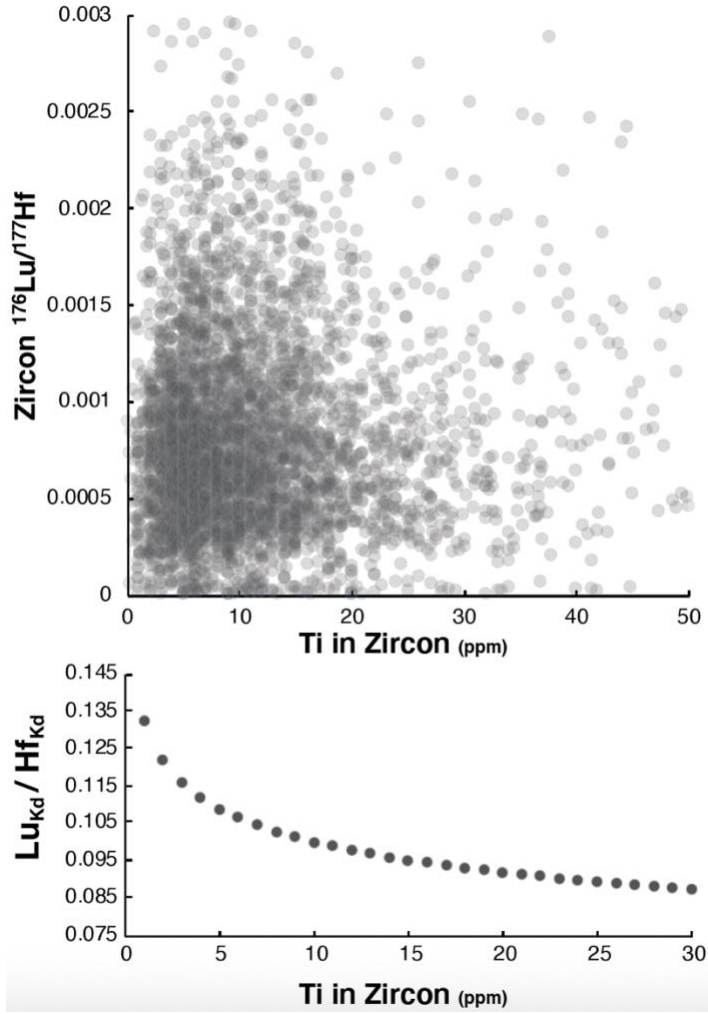


Fig. S7. Upper panel shows the Ti-in-zircon concentration against the zircon $^{176}\text{Lu}/^{177}\text{Hf}$ of >4,000 analyses from the global dataset. The lower panel shows the zircon/melt partition coefficient for the zircon Lu/Hf as a function of the Ti concentration. A variation from 5 to 25 ppm in Ti will not change the zircon $^{176}\text{Lu}/^{177}\text{Hf}$ by a factor greater than 1.5 times.

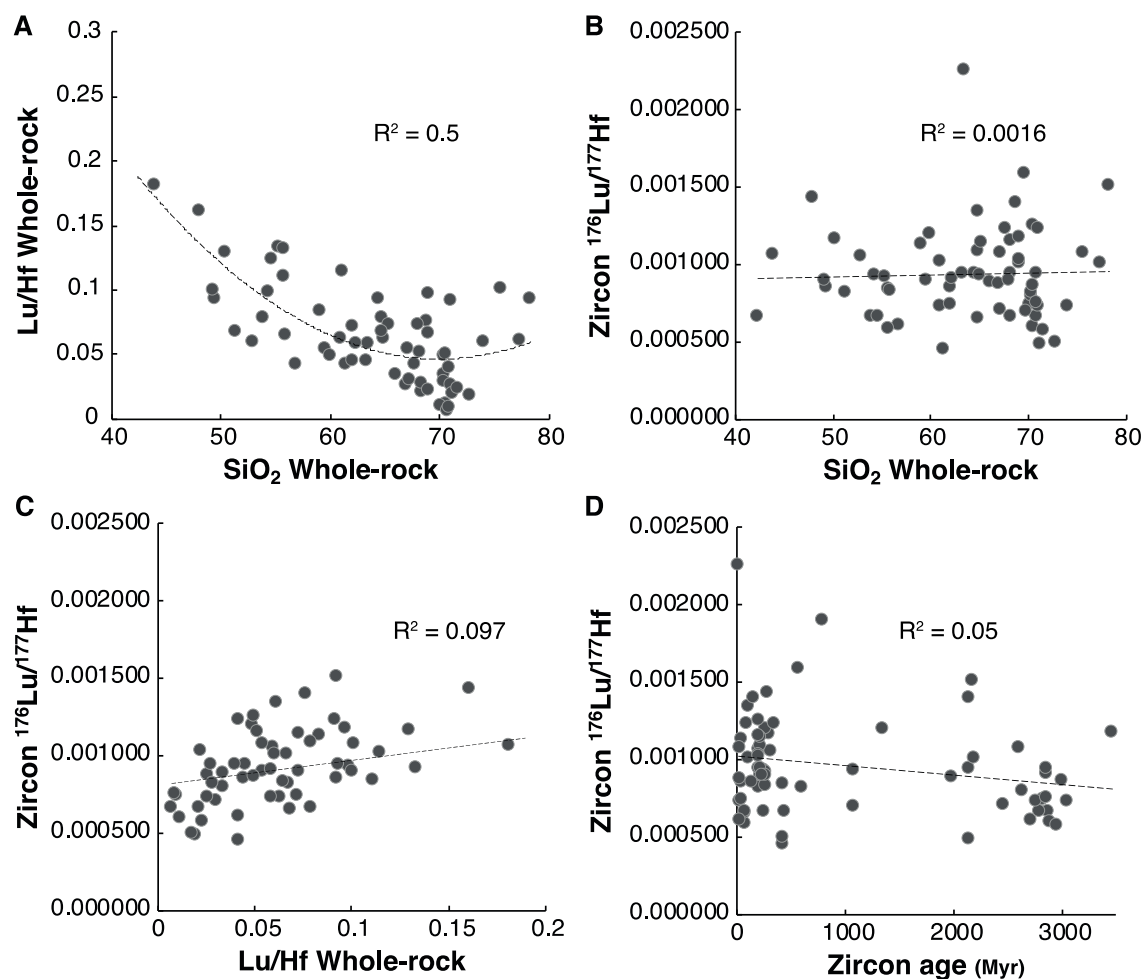


Fig. S8. Compositional control on Lu/Hf ratios. A) Whole-rock SiO_2 composition may correlate with whole-rock Lu/Hf ratios, but B) this correlation is not observed between whole-rock SiO_2 composition and zircon $^{176}\text{Lu}/^{177}\text{Hf}$. C) Correlation between Lu/Hf whole-rock and zircon $^{176}\text{Lu}/^{177}\text{Hf}$. D) Zircon $^{176}\text{Lu}/^{177}\text{Hf}$ ratios of samples studied with respect to crystallization age.

Table S1. Running median and metamorphic subtracted geomean of $^{176}\text{Lu}/^{177}\text{Hf}$ values obtained from the global zircon compilation of this study.

Row	Age (Myr) Median	$^{176}\text{Lu}/^{177}\text{Hf}$ isotopes						
		Median	Filtered Median	2 s.e.	Age (Myr) Geomean	Geomean	+2 s.e.	-2 s.e.
1	53	0.001335	0.001279	0.000023	53	0.001481	0.000020	0.000020
2	145	0.001160	0.001125	0.000020	143	0.001245	0.000017	0.000017
3	250	0.001208	0.001164	0.000014	252	0.001237	0.000013	0.000013
4	337	0.001140	0.001110	0.000017	341	0.001186	0.000016	0.000016
5	453	0.001151	0.001112	0.000017	453	0.001181	0.000016	0.000016
6	549	0.000873	0.000824	0.000015	549	0.000999	0.000015	0.000015
7	633	0.000830	0.000805	0.000014	639	0.000916	0.000013	0.000013
8	756	0.001080	0.001040	0.000022	754	0.001146	0.000021	0.000021
9	832	0.001124	0.001082	0.000020	839	0.001174	0.000019	0.000019
10	953	0.000880	0.000850	0.000018	953	0.000948	0.000018	0.000017
11	1051	0.000836	0.000816	0.000015	1051	0.000918	0.000014	0.000013
12	1152	0.000800	0.000780	0.000014	1150	0.000855	0.000013	0.000013
13	1237	0.000820	0.000796	0.000020	1241	0.000887	0.000019	0.000019
14	1344	0.000979	0.000951	0.000026	1348	0.001027	0.000025	0.000024
15	1449	0.000961	0.000936	0.000022	1451	0.001000	0.000021	0.000020
16	1559	0.000940	0.000921	0.000024	1555	0.000996	0.000022	0.000021
17	1649	0.001056	0.001025	0.000023	1649	0.001099	0.000021	0.000020
18	1756	0.000939	0.000907	0.000017	1754	0.001006	0.000016	0.000016
19	1850	0.000740	0.000723	0.000014	1850	0.000845	0.000012	0.000012
20	1947	0.000620	0.000600	0.000016	1949	0.000745	0.000015	0.000015
21	2049	0.000743	0.000720	0.000016	2049	0.000814	0.000016	0.000016
22	2144	0.000780	0.000758	0.000016	2148	0.000844	0.000015	0.000015
23	2242	0.000775	0.000760	0.000028	2246	0.000839	0.000026	0.000025
24	2350	0.000698	0.000677	0.000020	2349	0.000778	0.000020	0.000020
25	2464	0.000639	0.000632	0.000016	2460	0.000718	0.000012	0.000012
26	2535	0.000707	0.000688	0.000010	2540	0.000764	0.000010	0.000010
27	2656	0.000693	0.000670	0.000012	2653	0.000760	0.000012	0.000012
28	2735	0.000748	0.000736	0.000014	2741	0.000812	0.000013	0.000013
29	2851	0.000847	0.000831	0.000022	2849	0.000892	0.000021	0.000020
30	2948	0.000920	0.000908	0.000038	2950	0.000985	0.000029	0.000028
31	3056	0.000950	0.000940	0.000033	3053	0.000974	0.000029	0.000028
32	3155	0.000925	0.000900	0.000027	3152	0.000929	0.000027	0.000026
33	3245	0.000956	0.000927	0.000022	3246	0.000991	0.000022	0.000022
34	3347	0.000910	0.000874	0.000023	3347	0.000945	0.000023	0.000022
35	3450	0.000937	0.000903	0.000025	3447	0.000967	0.000025	0.000024
36	3537	0.000916	0.000911	0.000036	3543	0.000959	0.000031	0.000030
37	3647	0.000868	0.000865	0.000048	3648	0.000894	0.000035	0.000034
38	3742	0.000803	0.000796	0.000034	3745	0.000839	0.000032	0.000031
39	3844	0.000815	0.000769	0.000046	3843	0.000837	0.000048	0.000046
40	3950	0.000795	0.000747	0.000068	3948	0.000880	0.000069	0.000064
41	4023	0.000820	0.000772	0.000063	4037	0.000919	0.000063	0.000059
42	4139	0.000819	0.000788	0.000074	4141	0.000863	0.000074	0.000068
43	4240	0.000816	0.000803	0.000156	4247	0.000950	0.000162	0.000139
44	4339	0.001511	0.001511	0.000793	4339	0.001140	0.001034	0.000542

Table S2. Running median of $\delta^{18}\text{O}$ values obtained from the global zircon compilation.

Oxygen isotopes - $\delta^{18}\text{O}$ (‰)				
Row	Age (Myr)	Median	Filtered Median	2 s.e.
1	72	6.5	6.5	0.1
2	133	6.7	6.8	0.1
3	233	7.6	7.6	0.3
4	352	6.2	6.2	0.3
5	430	7.2	7.2	0.2
6	549	7.4	7.4	0.2
7	629	7.4	7.4	0.2
8	768	5.1	5.1	0.2
9	814	5.9	5.9	0.2
10	961	6.7	6.7	0.2
11	1043	6.7	6.7	0.2
12	1156	6.9	6.9	0.2
13	1239	6.4	6.4	0.2
14	1336	6.2	6.2	0.2
15	1457	6.3	6.3	0.2
16	1501	6.5	6.5	0.2
17	1652	6.1	6.1	0.2
18	1762	6.1	6.1	0.3
19	1860	6.9	6.9	0.2
20	1939	6.9	6.9	0.3
21	2048	7.0	6.9	0.3
22	2146	6.2	6.2	0.2
23	2227	5.8	5.6	0.4
24	2337	6.2	6.2	0.5
25	2452	6.2	6.2	0.3
26	2539	6.0	6.0	0.2
27	2672	5.8	5.8	0.2
28	2724	5.5	5.5	0.1
29	2828	5.5	5.5	0.2
30	2944	5.8	5.8	0.3
31	3029	5.2	5.2	0.6
32	3152	5.6	5.6	0.2
33	3242	5.8	5.8	0.4
34	3380	6.5	6.5	0.2
35	3436	6.1	6.1	0.3
36	3560	5.8	5.9	0.4
37	3636	5.7	5.7	0.4
38	3754	5.8	5.9	0.2
39	3869	5.7	5.8	0.4
40	3946	5.9	5.9	0.3
41	4037	6.2	6.2	0.2
42	4140	6.3	6.3	0.2
43	4232	5.7	5.7	0.2
44	4328	5.6	5.6	0.5

Table S3. Running average of $\delta^{18}\text{O}$ and $^{176}\text{Lu}/^{177}\text{Hf}$ datasets of 0.1 Gyr intervals greater than 1 s.d. of the mean, which define anomaly periods with inverse correlation.

Anomaly age interval	$\Delta^{18}\text{O}$	2 s.e.	$\Delta^{176}\text{Lu}/^{177}\text{Hf}$	2 s.e.
62	-0.47	0.14	0.00009	0.000023
242	0.74	0.27	0.000006	0.000014
345	-0.84	0.29	0.000043	0.000017
549	0.74	0.17	-0.000154	0.000015
631	0.8	0.21	-0.000168	0.000014
762	-1.4	0.23	0.000120	0.000022
823	-0.46	0.25	0.000164	0.00002
957	0.44	0.25	-0.000064	0.000018
1943	0.31	0.32	-0.000141	0.000016
2234	-0.61	0.42	0.00005	0.000028
3042	-0.42	0.61	0.000039	0.000033
3347	0.52	0.2	-0.000029	0.000023
4139	0.37	0.2	-0.000136	0.000074
4236	-0.24	0.23	-0.000166	0.000156

Table S4. Breakpoints for datasets at maximum number of observations ($m = 6$).

Dataset	Structural breaks ($m = 6$) in age intervals (Gyr)					
$^{176}\text{Lu}/^{177}\text{Hf}$	0.633	1.237	1.850	2.464	3.056	3.742
Oxygen	0.629	1.239	2.048	2.672	3.242	3.869

Table S5. Significant changes in the median Lu/Hf ratios values divided in 0.1 Gyr bins using 1,000,000 bootstraps and CUSUM estimates and above 68% confidence level of change. Row key from Table S1.

*Last row was not considered for interpretation, as median is calculated based on 6 analyses.

Row	Conf. Interval	Conf. Level	From	To
6	(6,7)	90%	0.0011579	0.00093782
10	(9,10)	72%	0.00093782	0.00081042
14	(14,14)	94%	0.00081042	0.00094795
19	(19,19)	100%	0.00094795	0.00069632
29	(29,30)	100%	0.00069632	0.00084885
44*	(43,44)	98%	0.00084885	0.001511

Table S6. Significant changes in the median values of oxygen isotopes divided in 0.1 Gyr bins using 1,000,000 bootstraps and CUSUM estimates and above 68% confidence level of change. Row key from Table S2.

Row	Conf. Interval	Conf. Level	From	To
8	(7,8)	79%	7.0143	5.5
10	(10,10)	70%	5.5	6.7667
13	(13,13)	86%	6.7667	6.2667
19	(19,19)	86%	6.2667	6.8833
22	(22,22)	94%	6.8833	6
28	(28,28)	86%	6	5.51
33	(33,33)	78%	5.51	6.1333
36	(35,36)	94%	6.1333	5.83
41	(41,41)	97%	5.83	6.25
43	(43,43)	50%	6.25	5.55

Table S7. Significant changes in the median Lu/Hf ratios values divided in 0.1 Gyr bins using 1,000,000 bootstraps and CUSUM estimates and above 95% confidence level of change. Row key from Table S1.

Row	Conf. Interval	Conf. Level	From	To
6	(6,9)	96%	0.0011579	0.00090252
19	(17,19)	100%	0.00090252	0.00069632
29	(29,34)	99%	0.00069632	0.00089024

Table S8. Significant changes in the median of Oxygen isotopes divided in 0.1 Gyr bins using 1,000,000 bootstraps and CUSUM estimates and above 95% confidence level of change. Row key from Table S2.

Row	Conf. Interval	Conf. Level	From	To
23	(19,25)	100%	6.5841	5.8283

Table S9. Partition coefficients (D) used for trace element modelling.

Mineral Source	Opx	Cpx	Grt	Amp	Plg	Kfs	Qtz	Bt	Zr	Ap	Ilm	Ttn
Basalt												
Lu	0.42	0.56	21	1.56	0.053	-	-	0.7	-	-	-	-
Hf	0.22	0.263	0.25	1.02	0.031	-	-	2.1	-	-	-	-
Yb	0.34	0.581	20.9	1.07	0.039	-	-	-	-	-	-	-
TTG												
Lu	0.48	0.665	57	1.65	0.039	0.012	-	0.74	-	-	-	6
Hf	0.0755	0.212	0.57	0.69	0.015	0.034	-	2.1	-	-	-	2.65
Yb	0.0357	0.966	53	1.65	0.039	0.012	-	-	-	-	-	-
Granite												
Lu	0.527	3.308	34.69	5.015	0.069	0.0195	0.014	0.901	453	17	2.4	10
Hf	0.116	0.44	3.3	1.16	0.148	0.025	0.03	0.65	2085	0.73	2.49	2.65
Yb	1.157	3.97	41.68	6.63	0.069	0.021	0.017	0.826	359	19.6	2.78	2.65

Dataset S1 (separate file). Source data for Figure 1

Dataset S2 (separate file). Source data for Figure 2

Dataset S3 (separate file). Source data for Figure 3

Dataset S4 (separate file). Source data for Figure 4

Supplemental file S1 tables in Excel format (separate file).

SI References

Balica, C., Ducea, M.N., Gehrels, G.E., Kirk, J., Roban, R.D., Luffi, P., Chapman, J.B., Triantafyllou, A., Guo, J., Stoica, A.M. and Ruiz, J., 2020. A zircon petrochronologic view on granitoids and continental evolution. *Earth and Planetary Science Letters*, 531, p.116005.

Campbell, I.H. and Allen, C.M., 2008. Formation of supercontinents linked to increases in atmospheric oxygen. *Nature Geoscience*, 1(8), pp.554-558.

Christensen, N.I. and Mooney, W.D., 1995. Seismic velocity structure and composition of the continental crust: A global view. *Journal of Geophysical Research: Solid Earth*, 100(B6), pp.9761-9788.

Claiborne, L.L., Miller, C.F., Gualda, G.A., Carley, T.L., Covey, A.K., Wooden, J.L. and Fleming, M.A., 2018. Zircon as magma monitor: Robust, temperature-dependent partition coefficients from glass and zircon surface and rim measurements from natural systems. *Microstructural geochronology: Planetary records down to atom scale*, pp.1-33.

Condie, K.C., Pisarevsky, S.A. and Puetz, S.J., 2021. LIPs, orogens and supercontinents: The ongoing saga. *Gondwana Research*, 96, pp.105-121.

Bradley, D.C., 2011. Secular trends in the geologic record and the supercontinent cycle. *Earth-Science Reviews*, 108(1-2), pp.16-33.

Ferry, J.M. and Watson, E.B., 2007. New thermodynamic models and revised calibrations for the Ti-in-zircon and Zr-in-rutile thermometers. *Contributions to Mineralogy and Petrology*, 154(4), pp.429-437.

Gardiner, N. J., Johnson, T. E., Kirkland, C. L. & Smithies, R. H. Melting controls on the lutetium-hafnium evolution of Archaean crust. *Precambrian Res.* 305, 479-488, doi:10.1016/j.precamres.2017.12.026 (2018).

Ludwig, K. R. User's Manual for Isoplot Version 3.00. A Geochronological Toolkit for Microsoft Excel. *Berkeley Geochronology Center Spec. Pub. No. 4*, Berkeley, CA, USA (2003).

Pastor-Galán, D., Nance, R.D., Murphy, J.B. and Spencer, C.J., 2019. Supercontinents: myths, mysteries, and milestones. Geological Society, London, Special Publications, 470(1), pp.39-64.

Puetz, S. J. & Condie, K. C. Time series analysis of mantle cycles Part I: Periodicities and correlations among seven global isotopic databases. *Geoscience Frontiers* 10, 1305-1326, doi:- 10.1016/j.gsf.2019.04.002 (2019).

Rollinson, H. & Pease, V. Using Geochemical Data: To Understand Geological Processes. 2 edn, (Cambridge University Press, 2021).

Rubatto, D., 2017. Zircon: the metamorphic mineral. *Reviews in mineralogy and geochemistry*, 83(1), pp.261-295

Spencer, C.J., Cawood, P.A., Hawkesworth, C.J., Raub, T.D., Prave, A.R. and Roberts, N.M., 2014. Proterozoic onset of crustal reworking and collisional tectonics: Reappraisal of the zircon oxygen isotope record. *Geology*, 42(5), pp.451-454.

Taylor, R. J. M. *et al.* Experimental determination of REE partition coefficients between zircon, garnet and melt: a key to understanding high-T crustal processes. *Journal of Metamorphic Geology* 33, 231-248, doi:10.1111/jmg.12118 (2015).